remote sensing

MDPI

Article

Remote Sensing of Aerosol Optical Depth Using an Airborne Polarimeter over North China

Han Wang [1,*], Leiku Yang [1,*], Anjian Deng [1], Weibing Du [1,2], Pei Liu [1] and Xiaobing Sun [3,4]

1 School of Surveying and Land Information Engineering, Henan Polytechnic University, Jiaozuo 454000, China; daj@hpu.edu.cn (A.D.); dwb@hpu.edu.cn (W.D.); liupei@hpu.edu.cn (P.L.)
2 Department of Geomantic Engineering, Bülent Ecevit University, Zonguldak 67100, Turkey
3 Key Laboratory of Optical Calibration and Characterization, Chinese Academy of Sciences, Hefei 230031, China; xbsun@aiofm.ac.cn
4 Anhui Institute of Optics and Fine Mechanics, Chinese Academy of Sciences, Hefei 230031, China
* Correspondence: ms.h.wang@163.com or wanghan@hpu.edu.cn (H.W.); yanglk@hpu.edu.cn (L.Y.)

Received: 28 June 2017; Accepted: 20 September 2017; Published: 22 September 2017

Abstract: The airborne Atmosphere Multi-angle Polarization Radiometer (AMPR) was employed to perform airborne measurements over North China between 2012 and 2016. Seven flights and synchronous ground-based observations were acquired. These data were used to test the sensor's measurements and associated aerosol retrieval algorithm. According to the AMPR measurements, a successive surface-atmosphere decoupling based algorithm was developed to retrieve the aerosol optical depth (AOD). It works via an iteration method, and the lookup table was employed in the aerosol inversion. Throughout the results of the AMPR retrievals, the surface polarized reflectances derived from air- and ground-based instruments were well matched; the measured and simulated reflectances at the aircraft level, which were simulated based on in situ sun photometer observed aerosol properties, were in good agreement; and the AOD measurements were validated against the automatic sun-photometer (CE318) at the nearest time and location. The AOD results were close; the average deviation was less than 0.03. The MODIS AODs were also employed to test the AMPR retrievals, and they showed the same trend. These results illustrate that (i) the successive surface-atmosphere decoupling method in the retrieved program completed its mission and (ii) the aerosol retrieval method has its rationality and potential ability in the regionally accurate remote sensing of aerosol.

Keywords: aerosol optical depth; polarization; airborne observation; AMPR; North China

1. Introduction

Aerosol has an impact on the Earth's radiation budget and climate due to its absorption and its scattering of solar radiation [1]. Aerosol remote sensing is of great significance in the prevention and management of air pollution [2,3]. The monitoring of the physical parameters of aerosol and their spatial distribution is an important part of quantitative remote sensing [4,5].

The global distribution of aerosol over land and oceans can be obtained by satellite observation. The sensors of the Polarization and Directionality of the Earth's Reflectance (POLDER) have been verified at both the regional and global scale [6–8]. The aerosol production resolution of POLDER is about 20 × 20 km^2. Algorithms based on POLDER measurements to derive aerosol loadings were developed at different observational conditions [9,10]. The Moderate Resolution Imaging Spectroradiometer (MODIS) provides 10 × 10 km^2 aerosol optical depth (AOD) data over the global land and sea area [11–14]. The Multi-angle Imaging SpectroRadiometer (MISR) [15], the Ozone Monitoring Instrument (OMI) [16], the Spinning Enhanced Visible and InfraRed Imager (SEVIRI) [17,18], and the Visible Infrared Imaging Radiometer Suite (VIIRS) [19] are also representative

sensors used to derive the aerosol optical properties consistently. However, more detailed results are still needed for regional aerosol monitoring. An airborne radiometer can provide better spatial resolution and emergency observations [20,21], which are an important complement to satellite observations.

The land surface is more complex than the ocean surface and presents a larger range of reflectances. The diversity of the land surface makes it difficult to estimate the Bidirectional Reflectance Distribution Function (BRDF), which increases the uncertainty associated with aerosol retrieval [12,22]. The scattering of radiation by aerosols changes both the intensity and polarization of solar light. The normalized polarized radiation is sensitive to aerosol optical and microphysical properties. In addition, the polarized reflectance from the land surface is almost wavelength independent [23,24]. The development of polarized observation sensors also creates new opportunities for aerosol remote sensing over land [25,26].

The airborne downward looking multispectral micro-polarimeter (MICROPOL) is a single viewing angle prototype polarimeter [27]. It provides accurate polarized measurements in five spectral bands centered at 490, 670, 870, 1600, and 2200 nm. The MICROPOL has participated in several airborne campaigns with various surface types, aerosol loadings and types, and levels of solar radiation. In 2001, the MICROPOL airborne observations were dedicated to aerosol characterization over the Mediterranean Sea. Two days during the experiments were particularly relevant for maritime and mineral dust aerosol characterization. The flights on those two days were used to retrieve the properties of natural aerosols from MICROPOL and Lidar. The MICROPOL derived AOD was in excellent agreement with the coincident MODIS retrievals on both days. The effective radius retrieved by MICROPOL was also in good agreement with the value obtained from MODIS in the mineral dust case, while it was significantly underestimated by MICROPOL in the pure maritime case [28]. Between 2002 and 2005, seven flights were performed with the MICROPOL instrument integrated onto a lightweight aircraft in the North of France. The multiband polarized (MBP) algorithm was tested and verified. For the pollutant aerosol cases, the MBP approach retrieved AOD with an accuracy of 0.03 over both natural and urban surfaces [27].

The Research Scanning Polarimeter (RSP) provides multiple bands, multiple directions, and polarized observations [26,29]. Twelve flights were performed during the Aerosol Lidar Validation Experiment (ALIVE) in the Southern Great Plains in Oklahoma, USA. The RSP instrument used in this campaign was placed onboard an aircraft and acquired good quality data throughout all twelve flights performed between 12 and 22 September 2005. Data taken by the RSP instrument during ALIVE were analyzed, and the aerosol parameters were retrieved. In the RSP algorithm, measurements at 2250 nm are used to estimate the land surface polarized reflectance, and the aerosol optical properties are retrieved using an optimal estimation method [30]. The retrievals were within the combined uncertainties of the retrieval, the AERONET products, and the Total Ozone Mapping Spectrometer Aerosol Index [31,32]. The RSP has also been used for atmospheric correction and cloud detection [33–36]. The Polarimeter Definition Experiment (PODEX) gathered a new class of instruments that aimed to reshape the next generation of atmospheric science. The Airborne Multi-angle SpectroPolarimetric Imager (AirMSPI), the Passive Aerosol and Cloud Suite (PACS) polarimeter, and the RSP were employed in the PODEX to derive the aerosol [37] and cloud [38] properties.

The Directional Polarized Camera (DPC) instrument is a POLDER-type polarized camera. The wide field of view ($120^\circ \times 120^\circ$) enables it to measure the polarization and directionality of the solar radiation reflected by the Earth-atmosphere system over a wide range; thus one target can be detected at different times at different directions. The DPC covers the spectral interval of 400 to 900 nm with three polarized spectral bands (490, 665, and 865 nm) [39]. Between 3 and 4 December 2009, DPC observations were made over the Pearl River Delta, China. Using these data sets, Cheng et al. investigated the aerosol optical properties and obtained encouraging retrievals [20,40].

Hundreds of square kilometers are covered in haze every winter in North China. It is a densely populated and heavily polluted area. Environmental degradation and health problems

have become increasingly prominent in recent years in these areas. Scientists have investigated the source, distribution, and constituents of air pollutants [41–44]. Although in situ observations from ground-based sensors and global observations from space-based sensors have provided large amounts of data, higher spatial resolution, and emergency observations, there has been almost a complete absence of aerosol remote sensing. Thus, the airborne Atmosphere Multi-angle Polarization Radiometer (AMPR) was designed by the Anhui Institute of Optics and Fine Mechanics, Chinese Academy of Science (AIOFM-CAS). The instrument has a highly polarized reflectance detection accuracy [45]. Multi-angular, multi-spectral, and polarized data can be provided by the AMPR. In recent years, seven flight campaigns have been performed to obtain polarized measurements over Beijing, Tianjin, and Hebei (BTH). The BTH region is the industrial and economic center of North China, and it was also emphasised as the area to be investigated [46]. Preparatory work in aerosol retrieval from AMPR measurements used measured polarized reflectance at 1640 nm as the estimation of the surface reflectance by assuming that the surface reflectance is dominant at 1640 nm [21,47]. This paper employs the AMPR measurements to derive the aerosol optical properties by the successive surface-atmosphere decoupling method without a priori knowledge of the land surface.

2. Experiments

This section focuses on the Multi-scale Observation of Aerosol (MOBA) experiment and the data collected by the AMPR instrument during the experiment in North China. The main purpose of the MOBA campaign was to acquire air- and ground-based observations to characterize the atmospheric aerosol from AMPR, Lidar, and the AERONET sun-photometer (CE318). The Chinese aircraft Yun-12 (Y12) participated in this campaign. Seven flights were conducted during the campaign to perform aerosol observations. The Y12 was equipped with the Lidar and AMPR, while the CE318 instruments were positioned in ground stations. The main characteristics of the flights during the MOBA experiment are reported in Table 1, where θ_v is the viewing zenith angle and ϕ is the relative azimuth angle. UT refers to the Universal Time.

Table 1. Characteristics of the flights performed during the Multi-scale Observation of Aerosol (MOBA) experiment.

Flight	Date	Time (UT)	Flight Altitude (km)	Area	Viewing Angles	AOD (Aeronet Level 1.5, 670 nm)	Atmospheric Characteristics
1	2012-08-10	01:49–02:53	3.1	117.3°–118.6°E 38.9°–39.21°N	$0 \leq \theta_v \leq 38$ $0 \leq \phi \leq 180$	0.24 (Caofeidian)	Thin haze
2	2012-08-10	05:06–06:47	3.2	117.3°–118.6°E 38.9°–39.21°N	$0 \leq \theta_v \leq 38$ $0 \leq \phi \leq 180$	0.11 (Caofeidian)	Clear
3	2013-04-29	02:31–04:38	3.7	117.3°–118.6°E 38.9°–39.21°N	$0 \leq \theta_v \leq 38$ $0 \leq \phi \leq 180$	0.23 (Caofeidian)	Clear
4	2013-04-30	01:31–04:00	3.7	117.3°–118.6°E 38.9°–39.21°N	$0 \leq \theta_v \leq 38$ $0 \leq \phi \leq 180$	0.14 (Caofeidian)	Clear
5	2013-05-01	01:53–04:18	3.7	117.3°–118.6°E 38.9°–39.21°N	$0 \leq \theta_v \leq 38$ $0 \leq \phi \leq 180$	0.33 (Caofeidian)	Thin haze
6	2014-09-18	03:31–04:48	3.7	116.5°–118.5°E 39.02°–39.96°N	$0 \leq \theta_v \leq 36$ $0 \leq \phi \leq 180$	0.15 (Caofeidian) 0.19 (Fengnan) 0.45 (Yutian) 0.32 (Baodi)	Thin haze
7	2016-11-13	03:55–06:37	3.1	114.3°–116.6°E 38.03°–39.98°N	$0 \leq \theta_v \leq 35$ $0 \leq \phi \leq 180$	-	Haze

2.1. Instruments

The MOBA campaign employed a multitude of instruments (Table 2) on aircraft and land sites. The ground stations of Caofeidian (39.18°N, 118.34°E), Fengnan (39.55°N, 118.10°E), Yutian (39.67°N, 117.67°E), and Baodi (39.71°N, 117.30°E) are located in BTH. They were equipped with automatic CE318s and provided the spectral AOD, the aerosol complex refractive index, and the particle size

distribution between 0.05 and 15 μm [48]. Measurements of the vertical distribution of the scattering layer were performed using the Lidar positioned on Y12 (Figure 1). The Lidar provided backscattering information of atmospheric molecules and aerosols at 532 nm. Images of the underlying surface were acquired by a charge-coupled device (CCD) camera, from which the type of land surface can be distinguished. A portable spectrometer (SVC HR-1024) was used to obtain an accurate reflectance of the land surface.

Table 2. Instruments used in the Multi-scale Observation of Aerosol (MOBA) experiment.

Instrument	Brief Introduction
AMPR	Multispectral polarimeter (Anhui Institute of Optics and Fine Mechanics (AIOFM), Hefei, China)
Lidar	Active atmospheric back scattering detector (AIOFM)
SVC HR-1024	Portable spectrometer (Spectra Vista, Poughkeepsie, NY, USA)
CE318	Automatic sun-photometer (Cimel, Paris, France)
POS	Position and pose recorder (Applanix, Richmond Hill, ON, Canada)
CCD camera	Color camera (Sony, Tokyo, Japan)

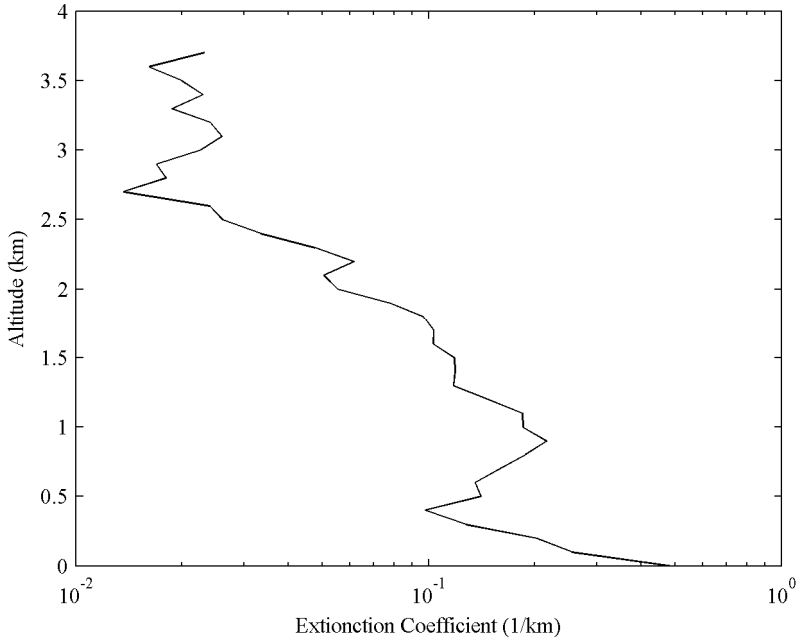

Figure 1. The profile of the aerosol extinction coefficient at 532 nm on 30 April 2013. The Lidar ratio of this sample was 34.2.

The polarized reflectance derived from the AMPR measurements was the focus of the study. The AMPR instrument (Table 3) uses two Wollaston prisms, which are fixed in a relative position, as polarization analyzers. The scanning of a scene occurs by means of a rotating polarization-insensitive two-mirror system that generally has its scanning plane oriented along the direction of travel of the aircraft. Four beams of linearly polarized light are derived from Wollaston prisms. This unique design allows the first three Stokes parameters (I, Q, and U) to be measured simultaneously in six spectral channels for each viewing angle. The normalized and polarized radiation and its intensity can be derived from the Stokes parameters. This design ensures that the spectral and polarimetric measurements in each instantaneous field of view (IFOV) detect the same scene even when the underlying surface varies rapidly or when the aircraft is moving. Limited by the size of the downward window, 67 out of a possible 111 viewing angles were available for each scan during the MOBA field experiment. For the 1° contiguous IFOVs of the AMPR, a limb-to-limb viewing angle range of FOV is provided. The scanning period of the AMPR is adjusted so that successive nadir views are one

IFOV apart and the same point at the ground is seen from multiple viewing angles. The AMPR is equipped with a standard light source to monitor the status of the sensor. In a complete scanning period, the AMPR takes about 1/3 of the overall time to acquire the target information, with the remaining time was used for the dark current measurement and onboard calibration. The centers of the AMPR spectral bands were 490, 555, and 665 nm for visible light, where scattering by molecules and submicron aerosols is significant; 865 and 960 nm for near-infrared light where scattering by fine-mode and coarse-mode aerosols predominates; and 1640 nm for shortwave infrared light, which is dominated by coarse-mode aerosol scattering. The radiant measurement has a wide dynamic range (the effective number of bits is 14) and a high signal-to-noise ratio (10^2 to 10^3). For the measurements used during the MOBA campaign, the radiometric and polarimetric calibration uncertainties were below 5% and 0.5% for all bands, respectively.

Table 3. Atmosphere Multi-angle Polarization Radiometer (AMPR) parameters.

Parameter	Specification
Band/Width (nm)	490/28, 555/34, 665/46, 865/45, 960/38 and 1640/44
FOV/IFOV	−55°–+55°/1°
Optical aperture	12 mm
Detector	Si-Pin (<1100 nm), InGaAs (>1100 nm)
Dynamic range	14 bits
Data storage	Hard Disk Drive
Voltage/power	28 VDC/350 W
Volume/Weight	0.14 m^3/50 kg

2.2. Observations and Case Studies

The MOBA experiments took place between 10 August 2012 and 13 November 2016 over the BTH region. The typical continental monsoon climate makes it hot and rainy in summer but cold and dry in winter. The annual average temperature is 5 to 20 °C. The annual precipitation is 400 to 800 mm. The aerosols in Beijing and central Hebei were mainly from daily life and industrial combustion. Additionally, the marine aerosol sometimes spread over Tianjin and eastern Hebei. The campaign was designed to collect air- and ground-based remote sensing data using the group of sensors to perform an aerosol retrieval study and a preliminary monitoring of the aerosol distribution. Three routes were taken during seven flights. The first five flights were dedicated to aerosol characterization over Tianjin and Tangshan along the same route. The routes started from Tianjin Binhai airport and covered the area around Bohai Bay. Flight 6 was dedicated to aerosol characterization from Beijing to Caofeidian. The aircraft started from Tongzhou airport, and it was the base camp for this experiment. The last flight started from Shijiazhuang airport and observed the polarized atmospheric characteristics over Shijiazhuang, Baoding, and Beijing.

Both the airborne and ground-based observations were conducted simultaneously. The downward observation sensors, including the AMPR, the Lidar, and a CCD camera, were installed on the aircraft. The CE318s were distributed in various respective stations before the experiments. The SVC HR-1024 spectrometer, equipped with rotatable polarizers, was used to detect the surface polarized properties of the target zones. The AMPR instrument participated in this campaign and acquired good quality data throughout all seven flights. Figure 2 shows the experimental region and examples of flight track segments (30 April 2013, 18 September 2014, and 13 November 2016) performed during this campaign. The MODIS photographs from Terra were used as the background to show the experimental environment (https://earthdata.nasa.gov/labs/worldview/). The flights were performed with different aerosol loadings and sometimes were perturbed by haze and cloud. However, the scenes that were selected for the retrieval of aerosol were cloud free. The last flight was conducted on a hazy day, and the data were used to retrieve the AOD during the haze event. The type of land surface was determined from the underlying surface pictures taken by the CCD camera and the Normalized

Difference Vegetation Index (NDVI) from the AMPR. Vertical profiles of the aerosol properties were derived with the Lidar, and the amount of column water vapor was determined using the CE318 measurements and AMPR measurements at 960 nm. The AMPR data were acquired at altitudes from 3.1 to 3.7 km. The profiles from Lidar showed that the aerosol particles were located primarily between the altitudes of 0 and 3 km in the atmosphere; these results indicated that the flight altitudes in the MOBA experiments were appropriate. Some spiral ascents and descents were also recorded and were also used to study the vertical distributions of the aerosol properties. The AMPR scan was oriented perpendicular to the aircraft's track on the afternoon of 10 August 2012 (the second flight in Table 1). The perpendicular scanning mode turned the AMPR into a push-broom imager, and the multi-angle aerosol retrieval method degenerated into a single angle method. The large amount of data collected from these flights, including the clear sky and considerable haze burden, provided excellent conditions for validating the aerosol remote sensing products. The aircraft route was designed to cover the ground stations. To constrain the properties of aerosols that were close in space and time to those observed by the CE318s, files obtained near the transit time were used in the validation.

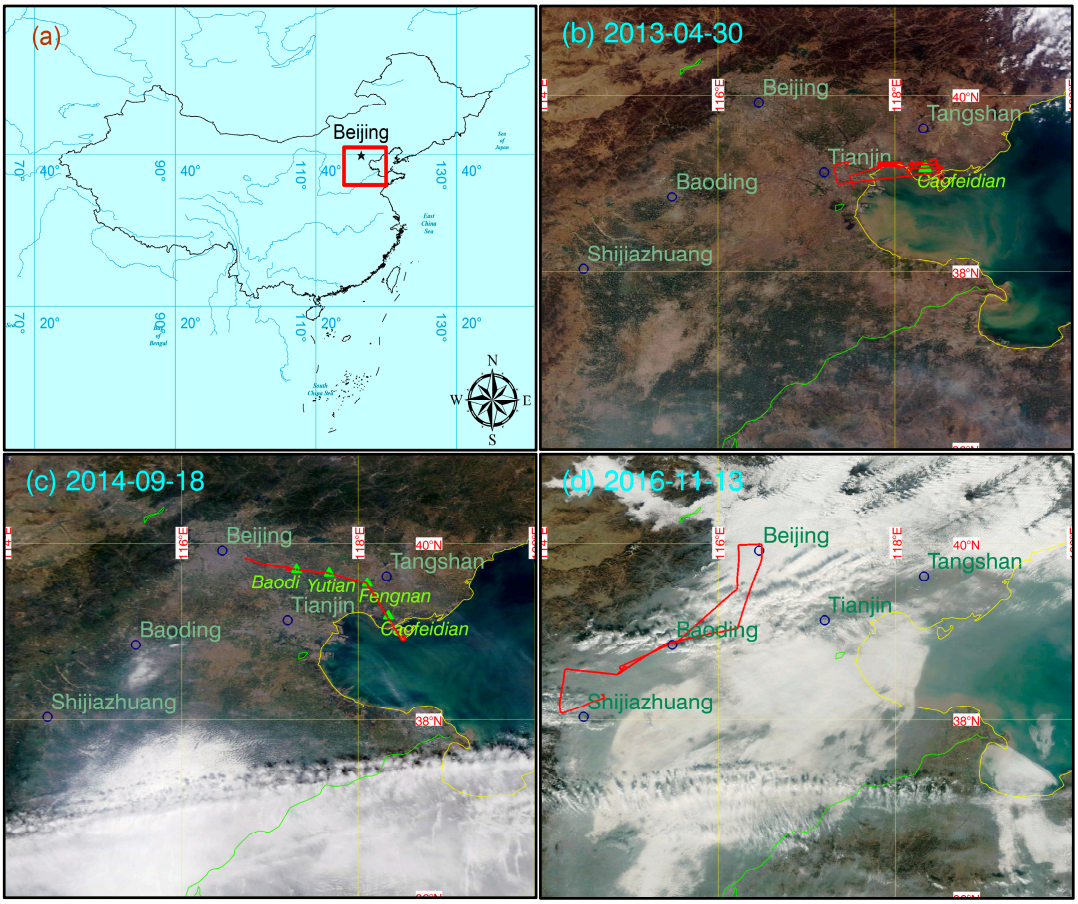

Figure 2. The geographical location of the experimental region (red quadrilateral in subgraph (**a**)) and flight track segments (red lines in subgraphs (**b**–**d**)). Subgraphs (**b**–**d**) cover the same area. The CE318 sites are indicated by green triangles.

During the MOBA campaign, the AMPR observed heterogeneous scenes consisting of vegetated surfaces and bare soil. To study the angular and spectral behavior of the polarized properties of the land surface observed during the campaign, we selected two zones. One of them was uniformly covered by vegetation, while the other was bare ground. The surface polarized reflectances were obtained accurately from the SVC HR-1024 spectrometer. The airborne and ground-based observations were conducted at the same time. Figure 3 shows some scans of polarized reflectances over a single

type of surface measured by the AMPR at 555, 665, and 865 nm as a function of the scattering angle. The repeated scattering angles, which were obtained from scanning near the back scattering direction, are not shown. It was found that, when the scattering angles were larger than 160°, the polarized reflectances at all three wavelengths lacked differentiation and were of larger noise. Measurements at this range were therefore not considered in the retrieval algorithm. It is important to note that the fluctuations in all spectral bands were strongly correlated. The spectral and angular behavior of the observed polarized reflectance was consistent with the observations reported in the literature [31,32].

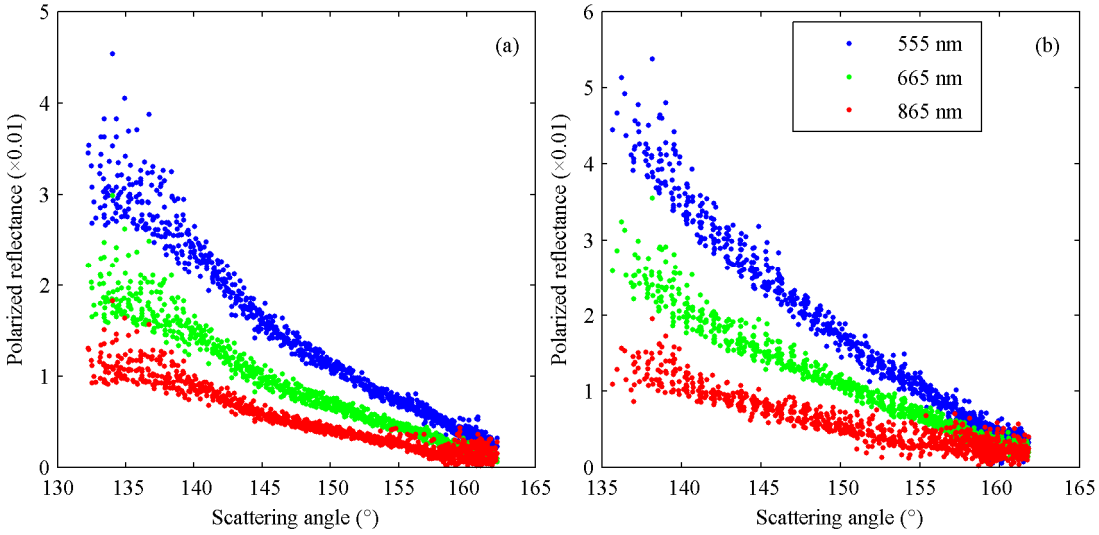

Figure 3. Polarized reflectances measured at the aircraft level as a function of the scattering angle over a (**a**) vegetated surface and (**b**) bare soil surface. The wavelengths of the data at 555, 665, and 865 nm are indicated by blue, green, and red dots, respectively.

3. Aerosol Retrieval Method

The retrieval scheme was built based on a lookup table approach. The radiative transfer model, RT3, [49] was used for the computation of the polarized radiation over the land surface. RT3 accounts for scattering by molecules and aerosol particles. As shown in Table 4, the lookup table computations were performed for several AOD (τ) values, a set of aerosol types, solar zenith angles θ_s, viewing zenith angles θ_v, and relative azimuth angles ϕ. The aerosol types consisted of six fine and six coarse modes derived by Lee and Kim [50] from AERONET sun-photometer observations over East Asia, including the region of North China. The aerosol size distribution followed a bimodal size distribution, consisting of two lognormal models, and was defined as a volume distribution.

$$\frac{d\,V(r)}{d\,\ln r} = \frac{C_f}{\sigma_{m,\,f}\sqrt{2\pi}} \exp\left[-\frac{\left(\ln r - \ln r_{m,f}\right)^2}{2{\sigma_{m,\,f}}^2}\right] + \frac{C_c}{\sigma_{m,\,c}\sqrt{2\pi}} \exp\left[-\frac{(\ln r - \ln r_{m,c})^2}{2{\sigma_{m,\,c}}^2}\right] \quad (1)$$

The subscripts f and c refer to the fine and coarse mode aerosols; r refers to the aerosol particle radius; C is the volume concentration ($\mu m^3/\mu m^2$); r_m denotes the mean radius of the number distribution; and σ_m is the geometric standard deviation of $\ln r$. Table 5 provides the σ_m, r_m , and the complex refractive indexes of different aerosol types. The complex refractive indexes (including the real part n and imaginary part k) were derived by reference to [50]. As reported in [51], the refractive index at 1640 nm was considered to be equal to 1020 nm, while, at 555 nm, it was calculated by linear interpolation. Here, we define $\eta = C_f/\left(C_f + C_c\right)$ as the fine mode fraction of aerosol, and this will be used later.

Table 4. Parameters of the lookup table.

Parameter	Values	No. of Values
τ	0.00, 0.05, 0.10, 0.20, 0.40, 0.80, 1.60, 2.50	8
θ_s	Interval [0°, 78°], with an increment of 2°	40
θ_v	0.00°, 6.97°, 12.76°, 18.51°, 24.24°, 29.96°, 35.68°, 41.40°, 47.12°, 52.84°, 58.56°, 64.28°, 69.99°, 75.71°, 81.43°, 87.14°	16
ϕ	Interval [0°, 180°], with an increment of 5°	37
η	Interval [0.0, 1.0], with an increment of 0.1	11

Table 5. Aerosol types used in the Atmosphere Multi-angle Polarization Radiometer (AMPR) retrieval.

Parameter	Type 1	Type 2	Type 3	Type 4	Type 5	Type 6
n_{555}	1.474	1.481	1.450	1.463	1.522	1.549
n_{665}	1.480	1.483	1.458	1.472	1.535	1.549
n_{865}	1.485	1.483	1.468	1.482	1.536	1.537
n_{1640}	1.481	1.476	1.468	1.481	1.528	1.525
k_{555}	0.0102	0.0086	0.0113	0.0100	0.0053	0.0036
k_{665}	0.0086	0.0074	0.0100	0.0088	0.0037	0.0024
k_{865}	0.0088	0.0078	0.0102	0.0090	0.0036	0.0023
k_{1640}	0.0091	0.0080	0.0104	0.0092	0.0036	0.0025
$r_{m,f}$	0.219	0.257	0.192	0.177	0.162	0.208
$\sigma_{m,f}$	0.531	0.535	0.504	0.474	0.538	0.619
$r_{m,c}$	2.724	2.580	2.915	2.256	2.286	2.241
$\sigma_{m,c}$	0.583	0.568	0.618	0.565	0.594	0.531

The optical properties of the aerosols were computed using Mie theory [52,53]. Prior to this, a fine mode and the corresponding coarse mode (the same cluster number) were combined by the weight of the fine mode fraction. τ can be written in the following form:

$$\tau = \int_{r_{min}}^{r_{max}} \pi r^2 Q_{ext}(\lambda; n, k, r) \frac{d\,V(r)}{d\,r} \mathrm{d}\,r \tag{2}$$

Q_{ext} is defined as the extinction coefficient, and can be calculated from Mie code, while λ refers to the wavelength. The AOD is interconvertible between certain band ranges through this function. Several discontinuous values of AOD from 0 (pure atmospheric molecular scattering) to 2.5 (turbid atmosphere scattering) were set. An interpolation method was used to cover the AOD between the discontinuous values. The scope of the sun zenith angle set in the lookup tables covered all of the observation conditions. The 16 discontinuous values of the viewing zenith angle were the Lobatto integral nodes. The relative azimuth angle was set with an appropriate scope and value to balance the accuracy and speed of calculation. A multidimensional interpolation method was used to approximate the polarized radiation corresponding to the actual viewing angles.

The main processes that generated the up-welling polarized reflectance for the surface-atmosphere reflection at the instrument level can be expressed as [31]:

$$\rho_\lambda^{cal} = \rho_\lambda^{atm} + (t_+\rho^{surf}t_- + T_+\rho^{surf}t_- + t_+\rho^{surf}T_- + T_+\rho^{surf}T_-) \tag{3}$$

The subscripts $+$ and $-$ refer to the downward and upward directions, respectively. T corresponds to the diffuse transmission of the atmosphere, while t is a direct transmission term. Equation (3) is arranged in order to separate the terms that contribute to the observed reflectance. The first term ρ_λ^{atm} describes the contribution of the upwelling light scattered from the atmosphere without interactions with the surface. ρ_λ^{atm} is the combination of aerosol (ρ_λ^{aer}) and molecular (ρ_λ^{mol}) polarized reflectance as given in Equation (4) [6]. μ_s refers to the cosine of the solar zenith angle, and τ_λ^{mol} refers to the

molecular optical depth. The second term, between brackets, describes the surface contribution transmitted directly through the atmosphere and the diffuse interactions between the land surface and the atmosphere.

$$\rho_\lambda^{atm} = \rho_\lambda^{mol} + \exp\left(-\tau_\lambda^{mol}/\mu_s\right)\rho_\lambda^{aer} \tag{4}$$

The combination of AOD and aerosol type was adjusted iteratively to minimize residual error. The combination that gave the smallest residual error (ε_{min}) was selected. For M wavelengths and N viewing angles, the residual error can be defined as Equation (5) [28]. λ_i is the ith wavelength; $\theta_{s,j}$, $\theta_{v,j}$, and ϕ_j are the jth viewing geometries; and $\rho_{\lambda_i}^{meas}$ stands for the measured polarized reflectance from the Stokes parameters.

$$\varepsilon = \sqrt{\sum_{i=1}^{M}\sum_{j=1}^{N}\left(\frac{\rho_{\lambda_i}^{cal}\left(\theta_{s,j},\theta_{v,j},\phi_j\right) - \rho_{\lambda_i}^{meas}\left(\theta_{s,j},\theta_{v,j},\phi_j\right)}{\rho_{\lambda_i}^{meas}\left(\theta_{s,j},\theta_{v,j},\phi_j\right) + 0.001}\right)^2 / MN} \tag{5}$$

The measurements at 960 nm were designed to acquire water vapor information and determine its significant contribution at this spectral band. Since this may result in errors in the estimation of the aerosol contribution, the radiation at 960 nm was not used in this retrieval scheme. The measurements at 490 nm were also not used because the polarized radiation was similar and there was more Rayleigh scattering than at 555 nm. Waquet et al. [23] studied the sensitivity of surface polarization reflectance to wavelength. As reported in [24], the surface polarized reflectance was very slightly wavelength dependent ($\mathrm{d}\rho_\lambda/\mathrm{d}\lambda \approx 10^{-6}\mathrm{nm}^{-1}$). This allowed different wavelengths to share the same surface polarization reflectance [19,27], which leads to about 2% of AOD error at 665 nm and is suitable. The AOD obtained in the nth loop was defined as $\tau_n (n \geq 1)$, with $\tau_{n+1} - \tau_n$ being the difference in the optical depth between adjacent loops. The program (Figure 4) could then be operated as follows:

1. Set $n = 1$ and $\rho^{surf} = \rho_{1640}^{meas}$;
2. Obtain the aerosol polarized reflectance from the lookup tables on the basis of viewing geometry angles and calculate the up-welling surface-atmosphere reflectance ρ_λ^{cal};
3. Calculate the residual error ε and the combination of AOD and aerosol type that gives the smallest residual error (ε_{min}) is selected as the expected retrieval;
4. Reobtain the polarized reflectance of the land surface ρ^{surf} from measurements at 1640 nm by atmospheric correction. If $n = 1$ go to step 2 and set $n = 2$, if $n > 1$ go to step 5;
5. Judge two propositions (explained in detail below) about the smallest residual error and the differences of optical depth. If both the propositions are true, the expected AOD τ_n is promoted to be the formal result and the program is ended. Otherwise, set $n = n + 1$ and restart from step 2.

λ indicates wavelengths of 555, 665, and 865 nm. In the first cycle, the program runs from step 1 to step 4. From the second circle, it starts running from step 2. Steps 2 and 3 describe the normal procedure of aerosol inversion using a lookup table method. ρ_λ^{aer} is obtained on the basis of actual viewing geometries from a lookup table. ρ_λ^{mol} is calculated exactly by the RT3 code, and ρ_λ^{cal} is obtained using Functions (3) and (4). Function 5 provides the residual error. In step 4, $\tau_{1640,n}$ is calculated from a combination of τ_n and aerosol type by Function (2). Then, the atmospheric correction program provides the ρ^{surf} on the basis of the combination at 1640 nm. Step 5 enables a judgement to be made to guide the retrieval. Two propositions, $\varepsilon_{\min} < 10^{-4}$ and $|(\tau_n - \tau_{n-1})/\tau_n| < 0.01$, were selected to ensure a reasonable retrieved result. The first proposition provides a standard by which to judge if the calculated and measured radiations are coincident. In general, the ε_{min} of the polarized reflectance at the top of the atmosphere is between about 10^{-4} and 10^{-3}, with 10^{-4} selected to guarantee the authenticity of the retrievals. The second proposition ensures that the retrieval process is convergent and provides the highest accuracy of retrieval. The $|(\tau_n - \tau_{n-1})/\tau_n|$value of 0.01 is a balance between the calculation speed and accuracy.

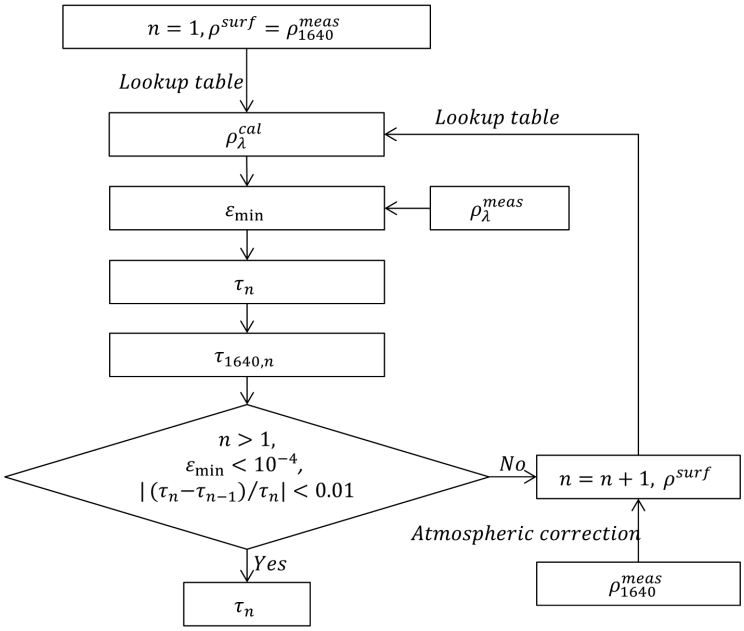

Figure 4. Flow chart of the AMPR algorithm.

4. Results and Analysis

The surface polarized reflectance and AOD were obtained simultaneously. The AMPR retrievals were compared with in situ observations to be validated. The verification of the surface polarized reflectance was used to examine the successive surface-atmosphere decoupling; a comparison between the measured and simulated polarized reflectances at aircraft level provided logical support to AMPR measurements; and the AOD validation was used to test the overall accuracy of the inversion.

4.1. Surface Polarized Reflectances

The measurements taken over the selected zones of vegetated and bare soil surfaces were studied in this section. A spectrometer, a polarizer, and a standard reflector can accurately obtain the surface polarization properties. The measurements were planned to start around the time when the AMPR flew over the target to ensure that the ground and airborne observations were performed under the same surface and solar radiation conditions. The spectrometer measurements were performed more than 10 times over a number of samples from each zone to achieve more accurate reflectance. These measurements were averaged to eliminate the nonuniformity of the surface. Measurements at six viewing angles, corresponding to six scattering angles, were obtained to describe the land surface properties. These polarized measurements reflected the angular and spectral response characteristics. The surface polarized reflectances were averaged between 550 and 870 nm due to the independence of the wavelengths. The spectral range is consistent with the AMPR bands. The airborne observed surface polarized reflectances were obtained by atmospheric correction. The vegetated and bare soil surface polarized reflectances from both the ground and airborne observations are plotted in Figure 5 as functions of the scattering angle. The surface polarized reflectances of both types of surface decreased as the scattering angle increased due to the impact of Fresnel's Law. The Nadal and Bréon [54] model results were also shown as a contrast with red lines. The Nadal and Bréon model followed the form of:

$$\rho^{surf} = \alpha[1 - \exp(-\beta \frac{F_p}{\mu_s + \mu_v})] \quad (6)$$

F_p is the Fresnel coefficient for polarized light. μ_v is the cosine of the viewing zenith angle. α and β are the empirical coefficients determined by the NDVI and ground type classification. The NDVI

was calculated based on the differences in reflectance at 665 and 865 nm. According to the NDVI and ground type of the two zones, α and β were designated as 0.95×10^{-2} and 120 for vegetated surfaces and 2.5×10^{-2} and 45 for bare soil surfaces, respectively. The surface polarized reflectances were well matched overall. This suggests that the surface-atmosphere decoupling used in the aerosol inversion program was reliable. Scattering angles bigger than 160° were not considered in this section for the reason referred to in Section 2.2.

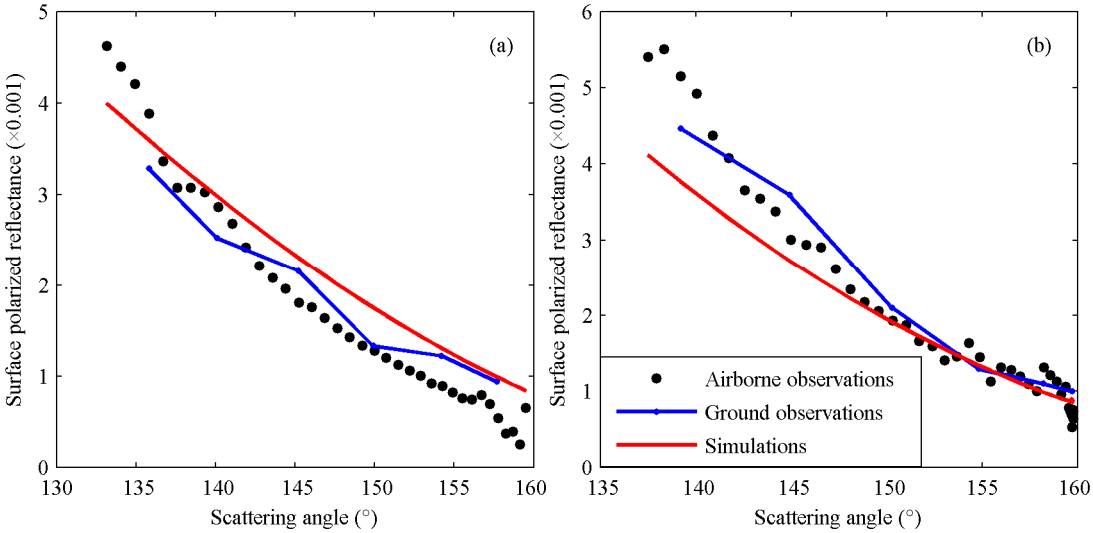

Figure 5. Surface polarized reflectances derived from ground observations (blue symbols and lines), airborne observations (black symbols), and simulations (red lines) as a function of the scattering angle over a (**a**) vegetated surfaces and (**b**) bare soil surfaces.

4.2. Polarized Reflectances at Aircarft Level

The AMPR measured polarized reflectances were selected to match the time when the aircraft was over the ground station. They were corrected by the absorption of trace gases and the scattering of atmospheric molecules. Eight samples from the measurements near the station were used to study the angular and spectral responses of reflectances at the aircraft level. The second flight was not considered for perpendicular scanning, and no multi-angular measurements were obtained. RT3 simulated the polarized reflectances. The aerosol optical and microphysical parameters used in simulations were derived from the CE318s. The surface polarized reflectances were provided by the atmospheric correction of the AMPR measurements. The measured and simulated reflectances are plotted at 555, 665, and 865 nm as a function of the scattering angle in Figure 6. The surface polarized reflectances did not play a major role at the aircraft level and had less and less influence on the observed polarized reflectance as the wavelength decreased. The magnitude of the behavior related to different samples was different for the different aerosol loadings, with a positive correlation (i.e., the subgraphs (d), (g), and (h) correspond to higher AODs, while (c) and (e) corresponded to lower AODs). The measured and simulated results agreed quite well (with a maximum difference of 2.53×10^{-5}), especially for scattering angles less than 145°.

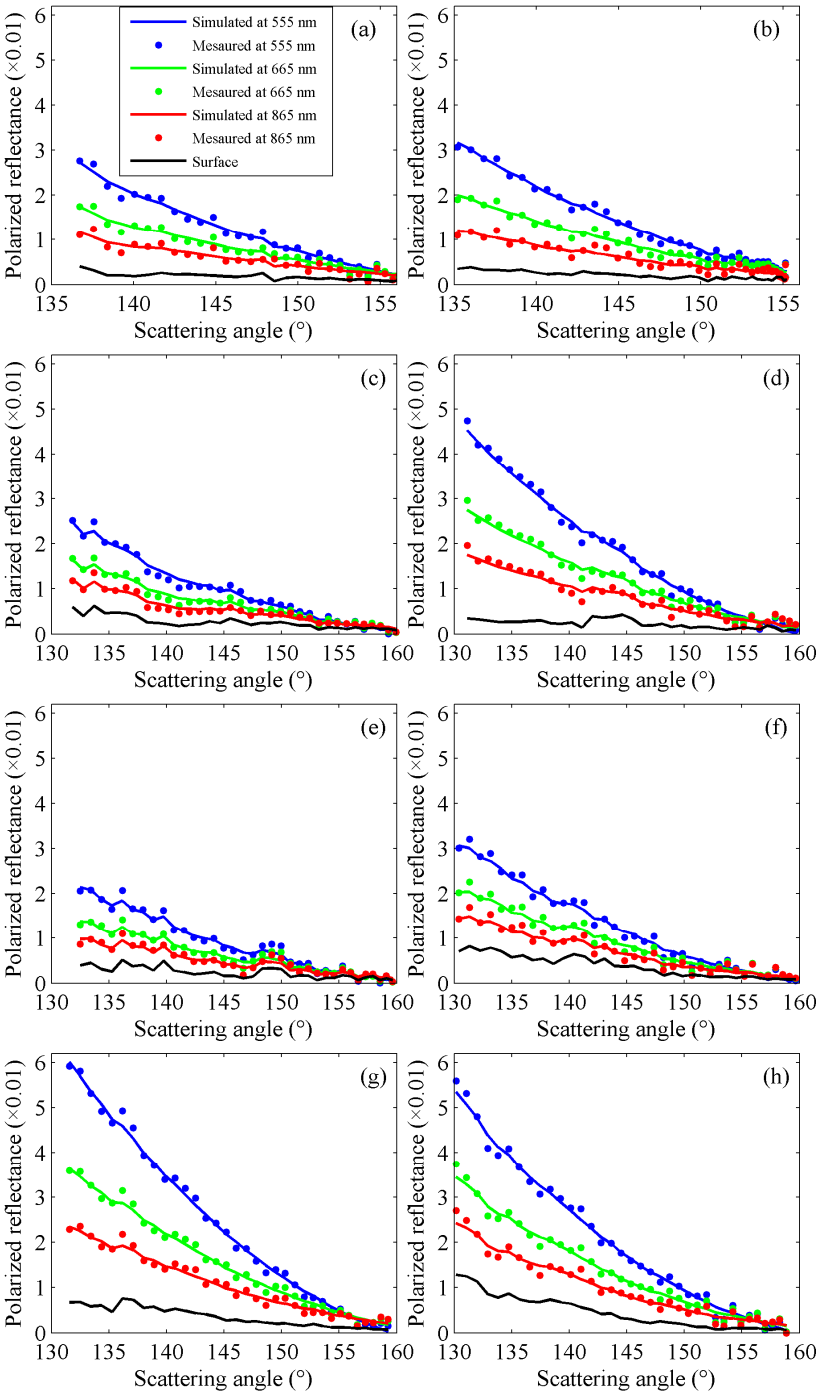

Figure 6. Measured (colored symbols) and simulated (colored lines) polarized reflectances at the aircraft level as a function of the scattering angle. (**a**–**h**) correspond to polarized reflectances over Caofeidian (flights 1, 3, 4, 5, and 6), Fengnan (flight 6), Yutian (flight 6) and Baodi (flight 6), respectively. The wavelengths of 555, 665, and 865 nm are presented in blue, green, and red, respectively. The land surface polarized reflectances are shown by black lines.

4.3. Aerosol Optical Depth

The retrieved AODs (665 nm) were assessed using the in situ measured AOD (670 nm) and the size distribution (Figure 7) obtained by the CE318s. The CE318s derived the AOD of a time-series with high precision. Benefitting from the reasonable design of a route, the CE318 and the nearest

(time and location) AMPR measurements were matched. Table 6 shows a comparison between the AODs from AMPR and the CE318s. The AMPR AOD values were systematically smaller, except for those calculated during the second flight, during which the scan was oriented perpendicular to the aircraft and the single angular retrieval method may have caused random error. The main causes of the results were: (i) polarized information from coarse particles may be missed in observations and inversions due to its weak polarized sensitivity and (ii) the depolarization of multiple scattering. However, the results from the AMPR and CE318s were close. The AMPR retrieved AODs along the route were matched with the MODIS images and eleven pairs of AODs were selected according to the transit time. Figure 8 provides the comparison between the AMPR retrieved AODs and the AODs from CE318 (a) and MODIS (b). The AMPR AOD trend was consistent with the CE318 and MODIS AOD production. The aerosol inversion errors gently increased with the increase of aerosol optical depth (Figure 9). The deviation was higher when the coarse particles were dominant. The deviation of Flight 5 (Caofeidian) was mainly caused by the wide range of its coarse mode. Both the fine and coarse mode size distribution of Flight 6 (Yutian) were bigger; thus the AOD was higher and more depolarization of multiple scattering lead to an error of 0.07. The deviation dispersed from 0.00 to 0.07 and the average error was about 0.03 through the nine verification points.

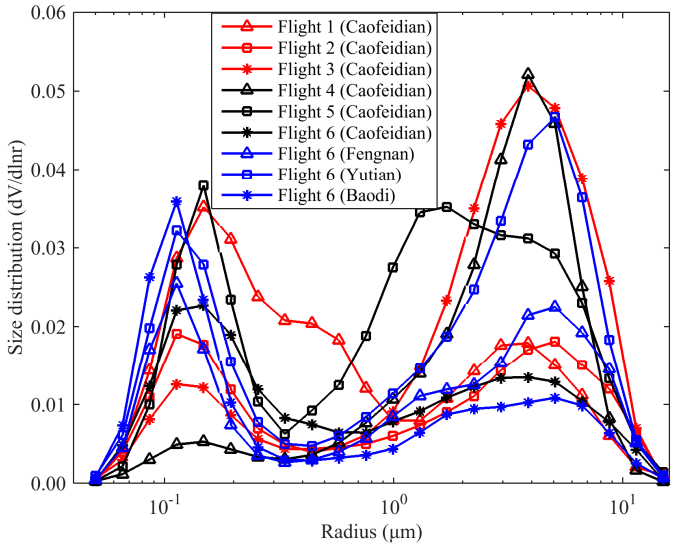

Figure 7. Aerosol size distribution derived from CE318 at the time of AMPR flying past. The contents between the brackets in the legend are the CE318 stations.

Table 6. Comparison between the aerosol optical depths (AOD) from the Atmosphere Multi-angle Polarization Radiometer (AMPR) and the CE318 sun-photometer.

Flight	Date (Station)	Time	CE318	AMPR (Averaged)	Deviation
1	2012-08-10 (Caofeidian)	02:33	0.24	0.22	0.02
2	2012-08-10 (Caofeidian)	06:22	0.11	0.15	0.04
3	2013-04-29 (Caofeidian)	03:12	0.23	0.20	0.03
4	2013-04-30 (Caofeidian)	02:24	0.14	0.11	0.03
5	2013-05-01 (Caofeidian)	02:38	0.33	0.28	0.05
6	2014-09-18 (Caofeidian)	03:35	0.15	0.14	0.01
6	2014-09-18 (Fengnan)	04:01	0.19	0.19	0.00
6	2014-09-18 (Yutian)	04:15	0.45	0.38	0.07
6	2014-09-18 (Baodi)	04:22	0.32	0.31	0.01

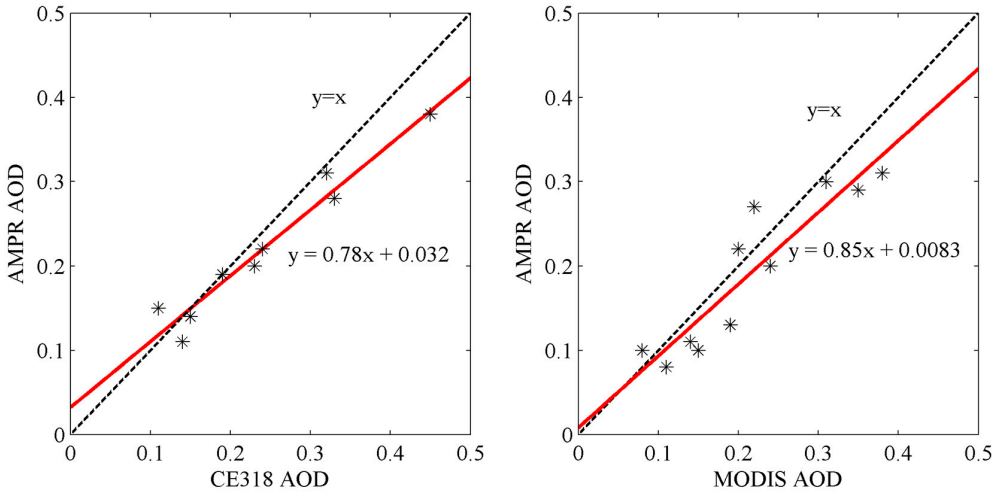

Figure 8. The AMPR retrieved AODs versus the CE318 and Moderate Resolution Imaging Spectroradiometer (MODIS) AODs.

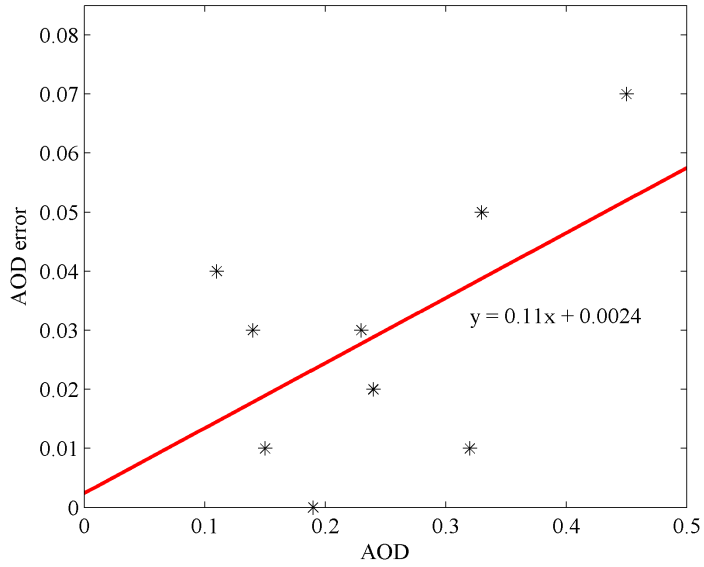

Figure 9. AOD errors as a function of AODs.

The retrieved AODs along the route are presented in Figure 10 together with the in situ AODs from the CE318s on a clear day (30 April 2013), a thin haze day (18 September 2014), and a haze day (13 November 2016). The AMPR results were averaged and reported over 10 s to clear random errors. The missing parts of the route correspond to measurements over urban areas and water bodies, as detected by the CCD camera, as well as non-convergence issues in retrieval. The AOD was dispersed from lower than 0.1 to near 0.85, with most aerosol loading cases included. The AODs over farmland near Caofeidian on 30 April 2013 are shown in Figure 10a. On the clear day, the AODs were slightly different and were below 0.2. On 18 September 2014, a thin haze pervaded Beijing and Tangshan. The AMPR started observations from an airport near Beijing, continued to Bohai Bay, and returned. The AODs obtained from 03:57 to 04:28 are presented in Figure 10b. These AODs show obvious variations over the time period. There was an obvious rise after 04:05 and a gentle descent after the aircraft flew over Yutian around 04:15. The results show a regional disparity. On the hazy day of 13 November 2016, haze and fog settled over North China. Although no in situ sun photometer measurements were recorded, we found the PM2.5 and PM10 in Baoding and Shijiazhuang. The PM2.5 and PM10 in Shijiazhuang on 13 November 2016 were 137 and 298 $\mu g/m^3$, respectively. In Baoding,

they were 187 and 277 μg/m^3, respectively. AODs were obtained from the north of Shijiazhuang (04:20) to the south of Baoding (04:45), where there was no cloud. The AOD was distributed between 0.7 and 0.85, and there was little regional disparity. The trend of AOD retrievals was consistent with the particulate matter measurements. The results show the ability of AMPR to retrieve AOD over heavy haze and to display the spatial distribution of aerosol.

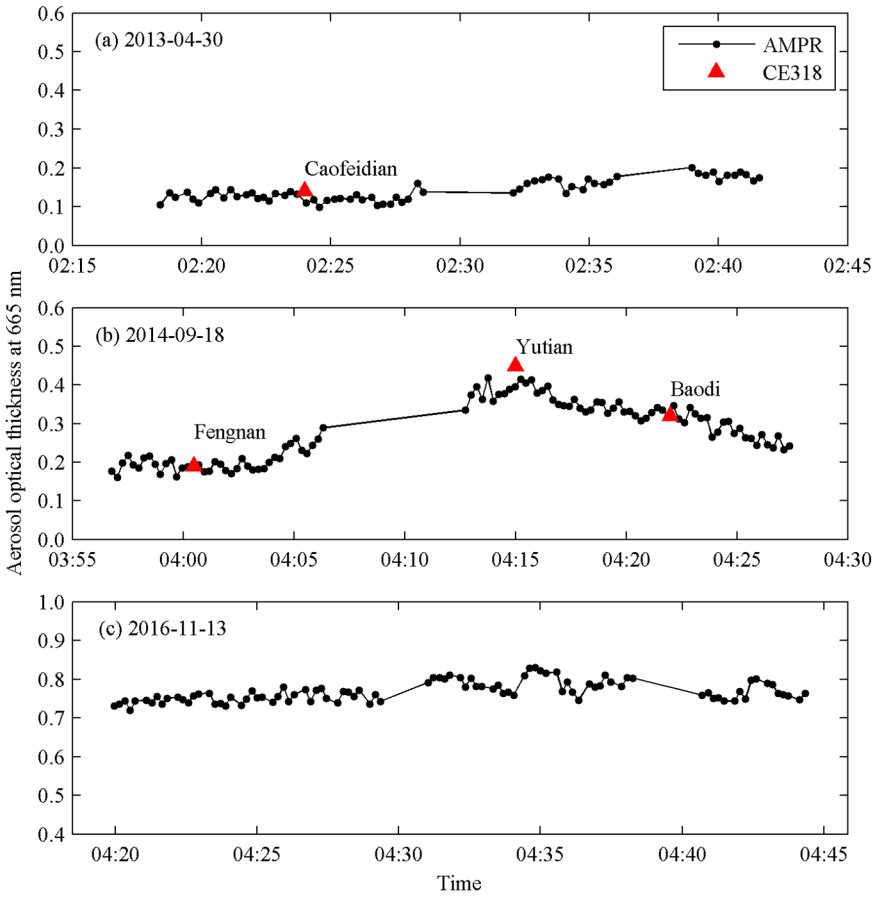

Figure 10. Aerosol optical depths (AOD) along the route, retrieved from the Atmosphere Multi-angle Polarization Radiometer (AMPR) at 665 nm, and the in situ AOD measured by a CE318 sun-photometer at 670 nm. The text in the figure indicates the CE318 station.

5. Conclusions

The MOBA campaign employed a multitude of instruments located on aircraft and land sites and was carried out from 2012 to 2016. The AMPR participated in the experiments many times as the main sensor. It was used to monitor the aerosol loading in North China. The long duration and large number of flights demonstrated the dependability of AMPR. In situ observations were synchronized with the airborne experiments. The CE318s and SVC HR-1024 played a useful supporting role in acquiring atmospheric and surface properties. A large amount of air- and ground-based data were obtained and analyzed. Data collected by the AMPR instrument during the experiment were used to study the aerosol optical properties with the help of Lidar and ground-based observations.

An aerosol retrieval algorithm was developed based on successive surface-atmospheric decoupling to retrieve the AOD from AMPR measurements without a priori knowledge of the land surface. Observations from seven flights over the BTH region were used to analyze AOD and surface polarized reflectances. Two flat zones along the route were selected. One was uniformly covered by vegetation and the other by bare soil. We designed air- and ground-based observations over both the surfaces to obtain the surface polarized reflectances. The results indicated that the successive

surface-atmosphere decoupling method used in the aerosol retrieval method worked well. Then, CE318 AODs from the ground stations and MODIS measurements were used to validate the AMPR retrievals. The AMPR AOD values were systematically smaller, except for during the second flight. The average error for the nine verification points was about 0.03, with the AOD below 0.45. The depolarization is higher when the aerosol loading is larger. That is why the AOD was lower than expected. The aerosol inversion errors gradually increased with the increase of optical depth and the trend of AMPR retrieved AOD was consistent with the CE318 and MODIS AOD production. The measured and simulated polarized reflectances at the aircraft level were also in good agreement. Aerosol retrieval on a haze day was also attempted, and encouraging results were obtained. The results indicate the promising future of AMPR to determine AOD over land whenever there is a significant aerosol burden and to provide more accurate estimates of aerosol optical depth without a priori knowledge of the land surface.

We demonstrated the ability of AMPR to (i) acquire an accurate reflectance of the polarized radiation, (ii) use such reflectance to retrieve aerosol optical parameters, and (iii) show that the successive surface-atmosphere decoupling method is effective in aerosol retrieval. This algorithm provides fast AOD, but it could not provide as many parameters of aerosol as the Generalized Retrieval of Aerosol and Surface Properties (GRASP) method does [55,56]. The simultaneous inversion of AOD and other parameters is undergoing developments efforts. In future work, the sensitivity of AMPR observations to the polarization of various types of surface should be investigated. The polarized characteristics of an urban area are much more complex. Further observations and investigations over urban areas need to be performed in future studies.

Acknowledgments: This study was supported by the National Natural Science Foundation of China (Grant No. 41601392, 41401403, 41601364 and 41601450), the Open Foundation of the Key Laboratory of Optical Calibration and Characterization, Chinese Academy of Sciences (Grant No. 2017JJ-01), the Key Technology R & D Program of Henan Province (No. 162102310089) and the Doctoral Foundation of Henan Polytechnic University (No. B2016-14 and B2014-018).

Author Contributions: Xiaobing Sun conceived and designed the experiments; Han Wang performed the experiments, analyzed the data, and wrote the paper; Leiku Yang contributed analysis tools; and Anjian Deng, Weibing Du and Pei Liu reviewed and edited the manuscript.

Conflicts of Interest: The authors declare no conflict of interest.

References

1. Kokhanovsky, A.A. Remote sensing of atmospheric aerosol using spaceborne optical observations. *Earth Sci. Rev.* **2013**, *116*, 95–108. [CrossRef]
2. Li, Z.Q.; Gu, X.; Wang, L.; Li, D. Aerosol physical and chemical properties retrieved from ground-based remote sensing measurements during heavy haze days in Beijing winter. *Atmos. Chem. Phys.* **2013**, *13*, 10171–10183. [CrossRef]
3. Sorek-Hamer, M.; Strawa, A.W.; Chatfield, R.B.; Esswein, R.; Cohen, A.; Broday, D.M. Improved retrieval of PM2.5 from satellite data products using non-linear methods. *Environ. Pollut.* **2013**, *182*, 417. [CrossRef] [PubMed]
4. Shmirko, K.; Bobrikov, A.; Pavlov, A. Atmospheric correction of satellite data. In Proceedings of the XXI International Symposium Atmospheric and Ocean Optics, Atmospheric Physics, Tomsk, Russia, 22–26 June 2015; p. 96803B.
5. Liang, T.; Sun, X.; Wang, H.; Ti, R.; Shu, C. Airborne Polarimetric Remote Sensing for Atmospheric Correction. *J. Sens.* **2015**, *2016*, 1–7. [CrossRef]
6. Deuzé, J.L.; Bréon, F.M.; Devaux, C.; Goloub, P.; Herman, M.; Lafrance, B.; Maignan, F.; Marchand, A.; Nadal, F.; Perry, G. Remote sensing of aerosols over land surfaces from POLDER-ADEOS-1 polarized measurements. *J. Geophys. Res. Atmos.* **2001**, *106*, 4913–4926. [CrossRef]
7. Deuzé, J.L.; Goloub, P.; Herman, M.; Marchand, A.; Perry, G.; Susana, S.; Tanré, D. Estimate of the aerosol properties over the ocean with POLDER. *J. Geophys. Res. Atmos.* **2000**, *105*, 15329–15346. [CrossRef]

8. Deuzé, J.L.; Bréon, F.M.; Deschamps, P.Y.; Devaux, C.; Herman, M.; Podaire, A.; Roujean, J.L. Analysis of the POLDER (POLarization and directionality of earth's reflectances) airborne instrument observations over land surfaces. *Remote Sens. Environ.* **1993**, *45*, 137–154. [CrossRef]
9. Waquet, F.; Cornet, C.; Deuzé, J.L.; Dubovik, O. Retrieval of aerosol microphysical and optical properties above liquid clouds from POLDER/PARASOL polarization measurements. *Atmos. Meas. Tech.* **2013**, *6*, 991–1016. [CrossRef]
10. Fan, X.; Chen, H.; Lin, L.; Han, Z.; Goloub, P. Retrieval of Aerosol Optical Properties over the Beijing Area Using POLDER/PARASOL Satellite Polarization Measurements. *Adv. Atmos. Sci.* **2009**, *26*, 1099–1107. [CrossRef]
11. Remer, L.A.; Kaufman, Y.J.; Tanré, D.; Mattoo, S.; Chu, D.A.; Martins, J.V.; Li, R.R.; Ichoku, C.; Levy, R.C.; Kleidman, R.G. The MODIS Aerosol Algorithm, Products, and Validation. *J. Atmos. Sci.* **2005**, *62*, 947–973. [CrossRef]
12. Levy, R.C.; Remer, L.A.; Kleidman, R.G.; Mattoo, S. Global evaluation of the Collection 5 MODIS dark-target aerosol products over land. *Atmos. Chem. Phys.* **2010**, *10*, 10399–10420. [CrossRef]
13. Levy, R.C.; Mattoo, S.; Munchak, L.A.; Remer, L.A. The Collection 6 MODIS aerosol products over land and ocean. *Atmos. Meas. Tech.* **2013**, *6*, 2989–3034. [CrossRef]
14. Hsu, N.C.; Jeong, M.J.; Bettenhausen, C.; Sayer, A.M.; Hansell, R.; Seftor, C.; Huang, J.; Tsay, S.C. Enhanced deep blue aerosol retrieval algorithm: The second generation. *J. Geophys. Res. Atmos.* **2013**, *118*, 9296–9315. [CrossRef]
15. Kahn, R.A.; Nelson, D.L.; Garay, M.J.; Levy, R.C.; Bull, M.A.; Diner, D.J.; Martonchik, J.V.; Paradise, S.R.; Hansen, E.G.; Remer, L.A. MISR Aerosol product attributes, and statistical comparison with MODIS. *IEEE Trans. Geosci. Remote Sens.* **2009**, *47*, 4095–4114. [CrossRef]
16. Curier, R.L.; Veefkind, J.P.; Braak, R.; de Leeuw, G.; Torres, O.; de Leeuw, G. Retrieval of aerosol optical properties from OMI radiances using a multiwavelength algorithm: Application to western Europe. *J. Geophys. Res. Atmos.* **2008**, *113*, 1161–1165. [CrossRef]
17. Wagner, S.C.; Govaerts, Y.M.; Lattanzio, A. Joint retrieval of surface reflectance and aerosol optical depth from MSG/SEVIRI observations with an optimal estimation approach: 2. Implementation and evaluation. *J. Geophys. Res. Atmos.* **2010**, *115*, 470–471. [CrossRef]
18. Popp, C.; Hauser, A.; Foppa, N.; Wunderle, S. Remote sensing of aerosol optical depth over central Europe from MSG-SEVIRI data and accuracy assessment with ground-based AERONET measurements. *J. Geophys. Res. Atmos.* **2007**, *112*, 88–97. [CrossRef]
19. Jackson, J.M.; Liu, H.; Laszlo, I.; Huang, H. Suomi-NPP VIIRS aerosol algorithms and data products. *J. Geophys. Res. Atmos.* **2013**, *118*, 12673–12689. [CrossRef]
20. Cheng, T.H.; Gu, X.F.; Xie, D.H.; Li, Z.Q.; Yu, T.; Chen, X.F. Simultaneous retrieval of aerosol optical properties over the Pearl River Delta, China using multi-angular, multi-spectral, and polarized measurements. *Remote Sens. Environ.* **2011**, *115*, 1643–1652. [CrossRef]
21. Wang, H.; Sun, X.; Sun, B.; Liang, T.; Li, C.; Hong, J. Retrieval of Aerosol Optical Properties over a Vegetation Surface Using Multi-angular, Multi-spectral, and Polarized Data. *Adv. Atmos. Sci.* **2014**, *31*, 879–887.
22. Yang, L.; Xue, Y.; Jie, G.; Kazemian, H.; Zhang, J.; Li, C. Improved Aerosol Optical Depth and Ångstrom Exponent Retrieval Over Land From MODIS Based on the Non-Lambertian Forward Model. *IEEE Geosci. Remote Sens.* **2014**, *11*, 1629–1633. [CrossRef]
23. Waquet, F.; Léon, J.F.; Cairns, B.; Goloub, P.; Deuzé, J.L.; Auriol, F. Analysis of the spectral and angular response of the vegetated surface polarization for the purpose of aerosol remote sensing over land. *Appl. Opt.* **2009**, *48*, 1228–1236. [CrossRef] [PubMed]
24. Wang, H.; Sun, X.; Sun, B.; Hong, J. Evaluation of Land surface polarization models based on airborne Advanced Atmosphere Multi-Angle Polarization Radiometer measurements. *ACTA Opt. Sin.* **2014**, *34*, 244–251. [CrossRef]
25. Deschamps, P.Y.; Breon, F.M.; Leroy, M.; Podaire, A.; Bricaud, A.; Buriez, J.C.; Seze, G. The POLDER mission: Instrument characteristics and scientific objectives. *IEEE Trans. Geosci. Remote Sens.* **1994**, *32*, 598–615. [CrossRef]
26. Cairns, B. Research scanning polarimeter and airborne usage for remote sensing of aerosols. *Proc. SPIE Int. Soc. Opt. Eng.* **2003**, *5158*, 33–44.

27. Waquet, F.; Goloub, P.; Deuzé, J.L.; Léon, J.F.; Auriol, F.; Verwaerde, C.; Balois, J.Y.; François, P. Aerosol retrieval over land using a multiband polarimeter and comparison with path radiance method. *J. Geophys. Res. Atmos.* **2007**, *112*, 71–81. [CrossRef]
28. Waquet, F.; Léon, J.F.; Goloub, P.; Pelon, J.; Tanré, D.; Deuzé, J.L. Maritime and dust aerosol retrieval from polarized and multispectral active and passive sensors. *J. Geophys. Res. Atmos.* **2005**, *110*, 95–100. [CrossRef]
29. Chenault, D.B. Research Scanning Polarimeter: Calibration and ground-based measurements. *Proc. SPIE Int. Soc. Opt. Eng.* **1999**, *3754*, 186–196.
30. Rodgers, C.D. *Inverse Methods for Atmospheric Sounding*; World Scientific: Singapore, 2000; p. 238.
31. Waquet, F.; Cairns, B.; Knobelspiesse, K.; Chowdhary, J.; Travis, L.D.; Schmid, B.; Mishchenko, M. Polarimetric remote sensing of aerosols over land. *J. Geophys. Res. Atmos.* **2009**, *114*, D01206. [CrossRef]
32. Cairns, B.; Waquet, F.; Knobelspiesse, K.; Chowdhary, J.; Deuzé, J.L. *Polarimetric Remote Sensing of Aerosols over Land Surfaces*; Springer: Berlin/Heidelberg, Germany, 2009; pp. 295–325.
33. Cairns, B.; Laveigne, J.D.; Rael, A.; Granneman, R.D. Atmospheric correction of HyperSpecTIR measurements using the research scanning polarimeter. In Proceedings of the Defense and Security, Orlando, FL, USA, 12–16 April 2004.
34. Elias, T.G.; Cairns, B.; Chowdhary, J. Surface optical properties measured by the airborne research scanning polarimeter during the CLAMS experiment. *Proc. SPIE Int. Soc. Opt. Eng.* **2004**, *5235*, 595–606.
35. Alexandrov, M.D.; Cairns, B.; Mishchenko, M.I.; Ackerman, A.S.; Emde, C. Characterization of cloud microphysical parameters using airborne measurements by the research scanning polarimeter. In *AIP Conference Proceedings*; American Institute of Physics: College Park, MD, USA, 2013; pp. 87–90.
36. Alexandrov, M.D.; Cairns, B.; Emde, C.; Ackerman, A.S.; Ottaviani, M.; Wasilewski, A.P. Derivation of cumulus cloud dimensions and shape from the airborne measurements by the Research Scanning Polarimeter. *Remote Sens. Environ.* **2016**, *177*, 144–152. [CrossRef]
37. Diner, D.J.; Xu, F.; Garay, M.J.; Martonchik, J.V. The Airborne Multiangle SpectroPolarimetric Imager (AirMSPI): A new tool for aerosol and cloud remote sensing. *Atmos. Meas. Tech.* **2013**, *6*, 2007–2025. [CrossRef]
38. Alexandrov, M.D.; Cairns, B.; Wasilewski, A.P.; Ackerman, A.S.; McGill, M.; Yorks, J.; Hlavka, D.; Platnick, S.; Arnold, G.T.; van Diedenhoven, B.; et al. Liquid water cloud properties during the Polarimeter Definition Experiment (PODEX). *Remote Sens. Environ.* **2015**, *169*, 20–36. [CrossRef]
39. Gu, X.; Chen, X.F.; Cheng, T.H.; Li, Z.Q.; Yu, T.; Xie, D.H.; Xu, H. In-flight polarization calibration methods of directional polarizedremote sensing camera. *Acta Phys. Sin.* **2011**, *60*, 707021–707028.
40. Gu, X.; Qiao, Y.; Wang, J.; Yu, T.; Cheng, T. High-resolution Directional Polarimetric Camera (DPC) used in the remote sensing of aerosol properties. *Proc. SPIE Earth Obs. Syst. XV* **2010**, *7807*, 55–65.
41. Yao, L.; Yang, L.; Yuan, Q.; Yan, C.; Dong, C.; Meng, C.; Sui, X.; Yang, F.; Lu, Y.; Wang, W. Sources apportionment of PM2.5 in a background site in the North China Plain. *Sci. Total Environ.* **2016**, *541*, 590–598. [CrossRef] [PubMed]
42. Chen, D.; Liu, X.; Lang, J.; Zhou, Y.; Wei, L.; Wang, X.; Guo, X. Estimating the contribution of regional transport to PM2.5 air pollution in a rural area on the North China Plain. *Sci. Total Environ.* **2017**, *583*, 280–291. [CrossRef] [PubMed]
43. Zhao, T.; Yang, L.; Yan, W.; Zhang, J.; Lu, W.; Yang, Y.; Chen, J.; Wang, W. Chemical characteristics of PM1/PM2.5 and influence on visual range at the summit of Mount Tai, North China. *Sci. Total Environ.* **2016**, *575*, 458. [CrossRef] [PubMed]
44. Zhang, L. Source attribution of PM2.5 pollution over North China using the adjoint method. In Proceedings of the AGU Fall Meeting, San Francisco, CA, USA, 15–19 December 2014.
45. Song, M.; Sun, B.; Sun, X.; Hong, J. Polarization calibration of airborne multi-angle polarimetric radiometer. *Opt. Precis. Eng.* **2012**, *20*, 1153–1158. [CrossRef]
46. Bilal, M.; Nichol, J.E. Evaluation of MODIS aerosol retrieval algorithms over Beijing-Tianjin-Hebei region during low to very high pollution events. *J. Geophys. Res. Atmos.* **2015**, *120*, 7941–7957. [CrossRef]
47. Qie, L.; Li, Z.; Sun, X.; Sun, B.; Li, D.; Liu, Z.; Huang, W.; Wang, H.; Chen, X.; Hou, W. Improving Remote Sensing of Aerosol Optical Depth over Land by Polarimetric Measurements at 1640 nm: Airborne Test in North China. *Remote Sens.* **2015**, *7*, 6240–6256. [CrossRef]
48. Dubovik, O.; King, M.D. A flexible inversion algorithm for retrieval of aerosol optical properties from Sun and sky radiance measurements. *J. Geophys. Res. Atmos.* **2000**, *105*, 673–696. [CrossRef]

49. Evans, K.F.; Stephens, G.L. A new polarized atmospheric radiative transfer model. *J. Quant. Spectrosc. Radiat. Trans.* **1991**, *46*, 413–423. [CrossRef]
50. Lee, K.H.; Kim, Y.J. Satellite remote sensing of Asian aerosols: A case study of clean, polluted and dust storm days. *Atmos. Meas. Tech. Discuss.* **2010**, *3*, 1771–1784. [CrossRef]
51. Wang, L.; Li, Z.Q.; Li, D.H.; Li, K.T.; Tian, Q.J.; Li, L.; Zhang, Y.; Lü, Y.; Gu, X.F. Retrieval of dust fraction of atmospheric aerosols based on spectra characteristics of refractive indices obtained from remote sensing measurements. *Spectrosc. Spect. Anal.* **2012**, *32*, 1644.
52. Bohren, C.F.; Huffman, D.R. *Absorption and Scattering of Light by Small Particles*; Wiley: Hoboken, NJ, USA, 1983; p. 448.
53. Grainger, R.G.; Lucas, J.; Thomas, G.E.; Ewen, G.B.L. Calculation of Mie derivatives. *Appl. Opt.* **2004**, *43*, 5386–5393. [CrossRef] [PubMed]
54. Nadal, F.; Breon, F.M. Parameterization of surface polarized reflectance derived from POLDER spaceborne measurements. *IEEE Trans. Geosci. Remote Sens.* **1999**, *37*, 1709–1718. [CrossRef]
55. Dubovik, O.; Herman, M.; Holdak, A.; Lapyonok, T.; Tanré, D.; Deuzé, J.L.; Ducos, F.; Sinyuk, A.; Lopatin, A. Statistically optimized inversion algorithm for enhanced retrieval of aerosol properties from spectral multi-angle polarimetric satellite observations. *Atmos. Meas. Tech.* **2010**, *4*, 975. [CrossRef]
56. Dubovik, O.; Lapyonok, T.; Litvinov, P.; Federspiel, C. GRASP: A versatile algorithm for characterizing the atmosphere. *SPIE Newsroom* **2014**. [CrossRef]